EXPERIMENTAL INVESTIGATION OF THE CROSS-SECTIONAL BENDING CAPACITY OF COLD-FORMED STEEL CHANNELS SUBJECT TO LOCAL-DISTORTIONAL BUCKLING INTERACTION

Jun Ye [1], Francisco J. Meza [2], Iman Hajirasouliha [3], Jurgen Becque [4], Paul Shepherd [5] and Kypros Pilakoutas [6]

Abstract: This paper describes an experimental programme carried out at the University of Sheffield to investigate the interaction of local and distortional buckling in cold-formed steel lipped channel beams. The channels were arranged in a back-to-back configuration and a total of six tests, including three different cross-sectional geometries, were completed. The specimens were tested in a four-point bending configuration with simply supported boundary conditions, while being laterally braced at the loading points. The beams were observed to fail in the constant moment span by interaction of local and distortional buckling. The geometric imperfections of the channels were recorded before the test using a specially designed measuring rig employing laser sensors. Tensile coupons were also extracted from the flat portions and the corner regions of the cross-sections in order to determine the material properties. Comparisons showed good agreement between the experimental results and the predictions of Eurocode 3, as well as those of the current AISI DSM provisions, whilst other DSM formulations based on the NLD and NDL concepts resulted in rather conservative predictions.

Keywords: Experiment; Cold-formed steel; Channel; Stability; Buckling; Local-Distortional Interaction.

[1] Research Associate, Dept. of Architecture & Civil Engineering, Univ. of Bath, Bath, BA2 7AY. Email: zjuyejun@gmai.com, j.ye@bath.ac.uk.

[2] PhD student, Dept. of Civil and Structural Engineering, Univ. of Sheffield, Sheffield, S1 3JD. Email: fjmezaortiz1@sheffield.ac.uk.

[3] Senior Lecturer, Dept. of Civil and Structural Engineering, Univ. of Sheffield, Sheffield, S1 3JD. Email: i.hajirasouliha@sheffield.ac.uk.

[4] Lecturer, Dept. of Civil and Structural Engineering, Univ. of Sheffield, Sheffield, S1 3JD. Email: j.becque@sheffield.ac.uk.

[5] Senior Lecturer, Dept. of Architecture & Civil Engineering, Univ. of Bath, Bath, BA2 7AY. Email: p.shepherd@bath.ac.uk.

[6] Professor, Dept. of Civil and Structural Engineering, Univ. of Sheffield, Sheffield, S1 3JD. Email: k.pilakoutas@sheffield.ac.uk.

1 Introduction

Cold-formed steel (CFS) beams are found in a wide range of applications and are particularly popular as secondary load-carrying members such as roof purlins, mezzanine floor joists and wall girts. In recent years, however, CFS beams have also been increasingly employed as primary structural elements in low- to mid-rise multi-storey buildings (Fiorino et al. 2014, Schafer 2011) and CFS portal frames with short to intermediate spans (Lim and Nethercot 2003, 2004). Storage racks are also routinely comprised of CFS members. Compared to their hot-rolled counterparts, CFS thin-walled members offer a number of advantages, such as a high strength-to-weight ratio, a relatively straightforward and flexible manufacturing process and an ease of transportation and erection. CFS also lends itself well to a modular (panelised) approach, resulting in high speeds of construction. On the other hand, the limited wall thickness of CFS members results in their ultimate capacity being governed by instabilities such as local, distortional and global buckling, while possible interaction between these buckling modes also has to be considered. While the global buckling modes are known to have negligible post-buckling capacity, members experiencing local buckling may exhibit significant post-buckling capacity before failure, a fact which is also to a lesser extent true for distortional buckling. Eurocode 3 (CEN 2006, CEN 2009) accounts for this post-buckling capacity by means of the 'effective with method', while the NAS and AS/NZS specifications also include the alternative Direct Strength Method (DSM) (AISI 2016, AS/NZS 2005).

Increasing demands on cold-formed steel sections in terms of efficiency and economy are leading to the fabrication of members with higher yield stresses to take advantage of the post-buckling reserve capacity available in the local and distortional buckling modes. However, this also increases the potential for coupled instabilities such as local-distortional interactive buckling. While local-flexural interactive buckling has been extensively studied experimentally and theoretically since at least the 1950s and -60s (e.g. Bijlaard and Fisher 1953, Van der Neut 1969, Graves Smith 1969), the study of local-distortional interaction has much more recent origins. The first observation that both buckling modes can simultaneously occur in CFS sections is credited to Kwon and Hancock (1992), who carried out compression tests on fixed-ended high-strength

CFS lipped channel sections with and without intermediate stiffeners in the web. The authors observed

significant post-buckling strength even when the flange buckled locally while also deforming in the

distortional mode and initially concluded that the simultaneous presence of both modes did not appear to

adversely affect the load carrying capacity. Further analysis of the test results was presented in (Kwon and

Hancock 1993) using the spline finite strip method. From a design perspective, Schafer (2002) proposed a

number of DSM variations aiming to account for mode interaction, among them the NLD approach, where

the strength reduction due to local-distortional interaction is taken into account by defining the slenderness

to be used in the DSM local strength equation on the basis of the ratio of the inelastic distortional capacity

to the (elastic) local buckling load. However, based on the available data he concluded that the NLD method

performed poorly and was overly conservative, adding that there was no evidence at that time that local-

distortional interaction was significant. It was not until more than 10 years after the first observations of the

possible coexistence of local and distortional buckling, however, that the potentially adverse nature of their

interaction was properly acknowledged by Yang and Hancock (2004), based on evidence obtained from tests

performed by the authors on high-strength CFS lipped channels with intermediate stiffeners in the web and

flanges, which were compressed between fixed-ends. The authors subsequently revived and supported the

NLD approach. Further experimental research on the interaction of local and distortional buckling in columns

was carried out by Yap et al. (2008), who tested an innovative cross-sectional shape designed to exhibit

several buckling modes at similar stress levels, including a local and two distortional modes. The NLD-DSM

design formula proposed by Yang and Hancock (2004) was further verified by Kwon et al. (2009) using

additional experimental results obtained from fixed-ended compression tests on high-strength CFS lipped

channels with intermediate stiffeners in the web or the flanges, as well as lipped channels without stiffeners.

These sections were designed to fail by interaction of local and distortional buckling and the ratio of the

distortional buckling stress to the local buckling stress (f_{crd} / f_{crl}) ranged from 0.7 to 4.1. Young et al. (2013)

also carried out compression tests on fixed-ended lipped channel columns designed to fail by local-

distortional buckling interaction. The columns were fabricated from different steel grades and exhibited

f_{crd}/f_{crl} ratios ranging from 1.1 to 1.7. The authors also investigated both the NLD and the symmetric NDL

approach to account for local-distortional interaction in design. The latter approach uses the DSM

distortional strength curve, but replaces the yield capacity in the definition of the distortional slenderness by

the inelastic local capacity. In the end a new DSM approach based on the NLD concept was proposed. This

new method was corroborated by the experimental data obtained by Dinis et al. (2014) on fixed-ended CFS

rack section columns affected by local-distortional interaction and exhibiting $f_{cr.D} / f_{cr,L}$ ratios between 1.31

and 1.46.

The interaction between local and distortional buckling has also been extensively studied numerically.

Silvestre et al. (2009, 2012), Dinis and Camotim (2015) and Martins et al. (2015, 2017a, 2017b) carried out

numerical simulations using finite elements of columns with lipped channel, hat, zed and rack cross-sections.

These studies revealed the f_{crd} / f_{crl} ratio to be one of the main factors affecting the reduction in ultimate

strength produced by the interaction between local and distortional buckling. Columns in which the local

and distortional buckling stresses of the section differed by less than 10% (referred to as a 'true interaction')

were found to be the most affected by local-distortional buckling interaction. For these columns Silvestre et

al. (2012) proposed complementing the DSM with the NDL approach. The NDL approach was further

assessed based on numerical simulations by Dinis and Camotim (2015) and Martins (2017b). In columns with

a relatively large difference between the local and distortional buckling stresses, 'secondary bifurcation' can

take place if the yield stress is considerably larger than the non-critical buckling stress. In the case where the

distortional buckling stress is considerably lower than the local buckling stress ($f_{crd} / f_{crl} < 0.8$), referred to as

'secondary local bifurcation', Martins et al. (2017b) found the effect of the interaction on the ultimate

strength to be negligible and the current DSM distortional strength curve was proven to provide adequate

predictions of the failure load. However, there still appears to be no consensus on the best approach to

predict the ultimate capacity of columns for which $f_{crd} / f_{crl} > 1.3$ ('secondary distortional bifurcation'), since

the detrimental effect of the local-distortional interaction in these columns cannot be ignored.

With respect to local-distortional interaction in members subject to bending a comparatively much smaller

volume of research work has been accomplished. Most of the previous research on beams has been

numerical, with hardly any experimental data available which is primarily focused on local-distortional interaction.

Laim et al. conducted four-point bending tests on plain and lipped channels arranged in a number of different built-up configurations connected with self-drilling screws, including back-to-back lipped channel I-beams. Parametric studies were conducted after validating an FE model in order to generate additional data. However, the failure modes and the nature of possible buckling interactions were not explicitly reported. The beams were unrestrained against lateral-torsional buckling. A comparison with the EN1993-1-3 design rules revealed safe predictions for the back-to-back lipped channels.

As part of a wider experimental programme into the structural performance of built-up sections Wang and Young (2016a) conducted three-point and four-point bending tests on back-to-back plain channels with web stiffeners, as well as back-to-back sigma sections. The specimens were screw-connected. Further numerical parametric studies were conducted (Wang and Young 2016b) where simultaneous local and distortional buckling was observed in a number of back-to-back sigma specimens. Nevertheless, the current DSM guidelines were found to be reliable for these cases, with an average ratio of the experimentally measured capacity to the predicted capacity of 1.04 (and a standard deviation of 0.05). Out of the eight specimens where local-distortional interaction was reported, two cases were found where this ratio was below 1.0, with values of 0.97 and 0.96.

Wang and Young (2015) also conducted four-point bending tests on back-to-back lipped channels with a web opening in the constant moment span.

Zhou and Shi (2011) carried out nine experiments on back-to-back lipped channels in four-point bending, followed by numerical studies. The channels were spot welded together at intervals of 300mm. The failure modes were unfortunately not reported. The research focused on presenting alternative effective width equations for back-to-back lipped channels.

In order to specifically study local-distortional interaction Dinis and Camotim (2010) carried out numerical simulations of lipped channel beams with two different cross-sections, one in which local buckling was triggered by the compression flange and another in which local buckling originated in the web. Each cross-section exhibited identical local and distortional buckling moments. The authors reported that the beams where local buckling started in the compression flange exhibited virtually no post-buckling reserve strength, while those beams where local buckling originated in the web were able to develop a fair amount of post-buckling capacity. Anbarasu (2016) proposed a modified DSM distortional strength curve to account for local-distortional buckling interaction in the case where the elastic local and distortional buckling moments are nearly equal, based on the results obtained from numerical models of lipped channel beams. Martins et al. (2017c) carried out a numerical investigation of CFS beams with three different cross-sectional shapes, with different support conditions and subject to uniform bending. All beams exhibited flange-triggered local buckling and possessed f_{crd} / f_{crl} ratios ranging from 0.5 to 2.00. A wide range of ratios of the yield stress to the non-critical buckling stress was also covered. The numerical results were subsequently used to assess the accuracy of the DSM when applied to beams failing in a local-distortional interactive mode. The researchers concluded that the current DSM strength curve for distortional buckling can only provide accurate estimates when the local buckling stress is noticeably larger than the distortional buckling stress ('secondary local bifurcation'), in which case local-distortional buckling interaction can be ignored. In the cases where both stresses are similar in magnitude or the distortional buckling stress exceeds the local buckling stress, the authors suggested a modification to the DSM formulas for beams using the same approaches as adopted for columns based on the NDL or NLD frameworks. Both approaches were found to yield good predictions.

Despite the various proposals to modify the DSM in order to account for the interaction between local and distortional buckling, the current DSM, as included in the NAS and AS/NZS specifications (AISI 2016, AS/NZS 2005), still does not address local-distortional interaction, with local-overall interaction being the only coupled instability currently accounted for. On the other hand, the effective width method, as stipulated in Eurocode 3 (CEN 2006, CEN 2009), does allow the possibility of combined local/distortional buckling, but at

the cost of a complex iterative process in which local and distortional buckling are accounted for by reducing the effective width of the compressed elements of the cross-section and reducing the effective thickness of the compressed internal and/or edge stiffeners, respectively.

This paper presents an experimental programme comprised of six CFS beams, each assembled from two lipped channels in a back-to-back configuration. The specimens were tested in laterally restrained four-point bending and were designed to fail by interaction of local and distortional buckling in the constant moment region. The back-to-back set-up was chosen to avoid the twist which inevitably takes place in single channels as a result of applying the load eccentrically relative to the shear centre. However, connectors were only provided over the supports and under the loading points, with none placed within the constant moment span, so that their presence and spacing would not affect the buckling pattern. The interaction between the channels (buckling in anti-symmetric patterns) was consequently kept to a minimum. The back-to-back configuration is a widely used test set-up, although alternative configurations have been used (e.g. Moen et al. 2013).

A comparison of the cross-sectional bending capacities obtained in the tests with those predicted by Eurocode 3 (CEN 2006, CEN 2009), the current AISI/ASNZ DSM provisions and a number of alternative DSM design approaches specifically developed to account for local-distortional buckling interaction, is also presented.

2   Section geometry and labelling

The specimens were assembled by connecting lipped channels in a back-to-back configuration. Three different cross-sectional geometries were considered, where the constituent channels had progressively deeper webs and narrower flanges, but all had the same cross-sectional area, i.e. all channels were fabricated by brake-pressing a pre-galvanized steel sheet with a width of 415 *mm* and a nominal thickness of 1.5 *mm.* The nominal thickness of the zinc coating was 0.04 *mm*. The back-to-back beams had a total length of 3300 *mm* and a distance between the end supports of 3100 *mm*. M12 zinc-plated bolts, tightened with a constant torque of 15 *Nm* (representative of hand-tightened 'snug' conditions), were used to connect the

individual channel sections through the web, as illustrated in Fig. 1. Connectors were provided under the loading points and over the end supports in order to ensure a uniform introduction of the load. Bolt holes with a diameter of 14 *mm* were drilled according to the lay-out illustrated in Fig.2.

Each test specimen was labelled according to its cross-section, using the letters *A*, *B* or *C,* with reference to Fig. 1*,* followed by the height of the cross-section in mm. As each test was repeated, the numbers 1 and 2 were used to differentiate between the first and the second of twin specimens. For each test specimen, the letters '*a*' and '*b*' were used to refer to the individual channels which formed the cross-section.

The cross-sectional dimensions of each channel were measured prior to their assemblage. Tables 1-3 list the measured dimensions of each test specimen, using the nomenclature established in Fig. 1. All reported values correspond to outer dimensions and they are the averages of several measurements taken along the length of the channels. The calculated second moment of area of the gross cross-section about the major axis is denoted by I_y and is also listed in Tables 1-3. The 0.04 mm zinc coating was deducted from the thickness to obtain these values.

The software package CUFSM (Schafer and Adany 2006), which implements the elastic finite strip method, was used to obtain the signature curves of the cross-sections under consideration. The results are shown in Fig. 3. The calculations were performed for a single channel (ignoring any interaction between the back-to-back channels), while using the nominal dimensions. In channel A the dimensions were chosen so that the local and distortional minima of the signature curve coincided exactly, with the aim of obtaining 'true' interaction and maximizing the effects of the local-distortional interaction mechanisms. Both local and distortional stresses were well below the yield stress. In channel B the distortional stress exceeded the local stress by a significant margin, but was still well below the yield stress. The section was designed to trigger secondary distortional bifurcation, where the distortional mode appears at some point in the post-buckling range of the local mode. Channel C again exhibited local and distortional stresses of very similar magnitudes, but with the distortional stress slightly preceding the local one. Both stresses were well below the yield stress.

The global branches of the signature curves in Fig. 3 can be ignored, since the study focused on the cross-sectional bending capacity of these sections and lateral restraints were in place during the test to prevent out-of-plane movement.

Table 4 lists the ratios of the elastic distortional buckling moment M_{crd} to the elastic local buckling moment M_{crl}, as well as the ratios of the local and distortional moments to the yield moment M_y. The elastic half-wave lengths associated with the local and distortional minima in the signature curve are also listed.

3 Material properties

A series of tensile coupon tests was carried out to determine the material properties of the test specimens. For each type of lipped channel one flat coupon was extracted from the center line of the web. Two corner coupons were also taken from the web-flange junctions in order to determine the effects of the cold-working process on the material properties. All coupons were taken from the end portions of test specimens after they were tested, as the beams were subject to strains in these regions which were low enough not to alter the material properties of the steel.

The flat coupons had a nominal gauge length of 57 mm and a width of 12.5 mm and each of them was instrumented with a 50 mm extensometer and two 5 mm strain gauges, one on each side of the coupon (Fig.4a). The corner coupons had a nominal gauge length of 57 mm and a width of 6 mm and were tested in pairs using V-shaped grips with a square bar with rounded corners placed in between the coupon ends (Fig. 4b). This avoided the need to flatten the coupon ends, which would have introduced unwanted bending moments into the coupons. Each pair of corner coupons was instrumented with a 50 mm extensometer and a 5 mm strain gauge attached to the outside of each coupon, as shown in Fig.4 (b).

The coupons were tested in accordance with the specifications of the relevant European standard ISO E. 6892-1 (2009). Table 5 lists the values of the material properties obtained for each flat coupon and each set of corner coupons, where E is the Young's modulus, f_y is the 0.2% proof stress, σ_u is the ultimate tensile strength and ε_f is the elongation after fracture, measured over a gauge length of 50 mm. For the pair of corner coupons belonging to section B270, the elongation after fracture reported in Table 5 is lower than for

the other corner coupons. This is due to the fact that the localization of the plastic deformations (necking) occurred slightly outside the gauge length and, therefore, this result should be disregarded. Figs. 5(a-c) presents both the measured engineering stress-strain curves and the true stress-strain curves, calculated using the following equations:

$$\sigma_{true} = \sigma\left(1+\varepsilon\right) \tag{1}$$

$$\varepsilon_{true} = \ln\left(1+\varepsilon\right) \tag{2}$$

In the above equations, σ and ε are the engineering stress and strain, respectively, based on the original cross-sectional area and the original gauge length of the coupons, and σ_{true} and ε_{true} are the true stress and the true strain, respectively. It is noted that Eqs. (1-2) are only valid as long as stresses and strains remain uniform over the gauge length or, in order words, up to the point where necking starts to develop. Therefore, the true stress-strain curves are only shown in Figs. 5(a-c) up to the point where the engineering curves show a peak.

4 Imperfection measurements

The stability of thin-walled CFS members may be significantly affected by initial geometric imperfections, especially when coupled instabilities are involved (e.g. van der Neut 1969, Dubina and Ungureanu 2002, Becque 2014). For this reason, the magnitude and shape of the imperfections of each specimen were recorded after the specimens were assembled, using the measuring set-up shown in Fig. 6. This set-up consisted of a traverse system with a laser sensor, mounted on a flat table and equipped with two electric motors which moved the sensor in two orthogonal directions along high precision bars, thus enabling it to cover a rectangular surface area. The laser was able to measure the distance to the surface of the test specimens with an accuracy of ±0.0075 *mm.* The ability of the traverse system to maintain a level measuring plane was verified against measurements of the nominally flat table in the absence of a test specimen. This flat table was guaranteed to be grade 3, which according to BS817 (2008) provided a surface with a deviation from flatness of less than 0.06 *mm*. During the measuring process, the laser sensor was moved longitudinally

at a speed of 5 *mm/s,* while readings were taken at a sampling rate of 5 Hz, resulting in one reading every millimetre.

For each specimen the out-of-plane imperfections were recorded along three lines on the webs and two lines on the flanges, as shown in Fig. 7. The convention was adopted that positive values indicate imperfections away from the centroid of the channel. Measurements taken along the web were used to obtain an order of magnitude of the local buckling imperfections, which was calculated by subtracting the average measurement taken along lines 1 and 3 from the measurements taken along line 2. Similarly, an indication of the imperfections affecting the distortional buckling mode was obtained from the measurements taken along the flanges by first subtracting the measurements taken along lines 4 and 7 from the measurements taken along lines 5 and 6, respectively. However, since the web could not be guaranteed to be perfectly vertical during the flange readings and any inclination of the web would strongly affect these readings, the amplitude of the distortional imperfection was reported as the maximum imperfection (calculated as explained above) relative to the average imperfection along the length of the specimen. The out-of-plane imperfections were only recorded along the constant moment span (in between the loading points) since the beams were designed to fail within this region.

Figs. 8-10 show the local and distortional imperfections obtained for a representative channel belonging to specimen groups A230, B270 and C180, respectively. Table 6 also lists the maximum values of the local and distortional imperfections of each channel. It can be seen that the maximum local imperfection of 0.41 mm was recorded in specimens B270, which had the most slender web. In channels A230, which displayed an intermediate web slenderness, the maximum local imperfection was 0.36 *mm*, while the maximum local imperfection measured in channels C180, with the least slender web, was only 0.1 *mm*. With respect to the distortional imperfections, the maximum recorded value of 0.38 *mm* was measured in channels A230, while the maximum distortional imperfections in channels B270 and C180 were 0.22 *mm* and 0.35 *mm*, respectively.

5 Test set-up

A total of six back-to-back channel beams were tested in a four-point bending configuration. The set-up is illustrated in Fig.11 (a). The specimens were supported on rollers located 3100 *mm* apart. All specimens were bent about their major axis. The loading system consisted of an actuator with a maximum capacity of 160 *kN,* which imposed the load through a spreader beam onto the test specimen at two discrete locations 1200 *mm* apart. The spreader beam was restrained against out-of-plane movement by a specially designed guidance system, which is shown in Figs. 11(b) and 12. Nylon blocks were used as bearing pads between the spreader beam and the uprights of the restraining assembly in order to reduce friction. A pin support on one end and a roller support on the other were used to transfer the load from the spreader beam to the specimen. These supports were also designed to restrain any out-of-plane displacement of the top flange of the test specimen through specially designed flanges, as shown in Fig. 12. Wooden blocks with a length of 250 *mm* were packed tightly into the cross-section at the loading points and end supports to avoid localized bearing failure, as shown in Figs. 12 and 13.

Three potentiometers with a stroke of 25 *mm* were placed under the test specimen at mid-span and under the two loading points in order to record the vertical deflections of the beam. Dial gauges were placed on the specimen at the supports to measure possible vertical support settlements.

A displacement controlled loading scheme with a constant rate of 1 *mm/min* was used for all test specimens. The tests were halted for 4 minutes slightly before the peak load was reached, in order to eliminate strain-rate dependent effects. The tests were then continued and eventually terminated when the load dropped below 20% of the peak load on the descending path.

6 Test results

6.1 Moment-deformation curves

Fig. 14 plots the bending moments against the mid-span deflections for all test specimens. The ultimate capacities of all test specimens are also listed in Table 7. In general, a good agreement was obtained within each set of twin specimens, with the ultimate capacities varying by less than 2% from each other. An

exception occurred in specimens B270, where the ultimate capacity of specimen B270-1 was considerably lower than that obtained for its counterpart. This was due to the fact that specimen B270-1 was tested without wooden blocks under the load application points. As a result, web crippling occurred under the loading points, in combination with a local buckling pattern which extended all along the constant moment span. Therefore, the results of test B270-1 should be disregarded.

The moment-curvature diagrams obtained from the tests are also shown in Fig. 15, whereby the constant curvature κ in the moment span was calculated using the following formula:

$$\kappa = \frac{2y}{y^2 + \left(\dfrac{L}{2}\right)^2} \tag{3}$$

In the above equation L (= 1200 mm) is the length of the moment span and y is the deflection at mid-span relative to the loading points, as shown in Fig.16:

$$y = v_2 - \frac{v_1 + v_3}{2} \tag{4}$$

In Fig. 15, the moment and the curvature are made dimensionless by relating them to the yield moment M_y and the curvature κ_y, defined as:

$$\kappa_y = \frac{M_y}{E \cdot I_y} \tag{5}$$

where E and I_y are the elastic modulus and the second moment of area of the gross cross-section about its major axis, respectively.

6.2 Failure modes

All test specimens (with the previously noted exception of specimen B270-1) were observed to fail within the constant moment span by interaction of local and distortional buckling.

In specimens A230 simultaneous local and distortional buckling was observed resulting from true interaction. With respect to local buckling, the web was the most slender component of the cross-section,

which explains why the local buckling pattern was much more obvious in the web than in the flanges, as seen in Fig. 17. As previously pointed out by Dinis and Camotim (2010), this limits the severity of the interaction. The onset of buckling was determined from the moment-curvature diagram previously introduced in Fig. 15 and presented in more detail for the A230 specimens in Fig. 18(a). The initial slope of the diagram is close to 1.0, indicating a fully effective elastic cross-section. However, an abrupt change of the stiffness is observed at a moment of 18.5 kNm in both specimens A230-1 and A230-2 (corresponding to a moment of 9.25 kNm in each individual channel). Since the stresses in the cross-section are still well below yielding at this load level, the sudden change in stiffness can only be attributed to cross-sectional instability. A comparison between the buckling moments thus determined from the experimental data and the ones obtained from the finite strip method (Fig. 3) is presented in Table 8 (for single channels). Pictures of the A230-2 specimen at progressive stages of deformation are shown in Fig. 19. As seen in Fig. 18(a), the A230 specimens displayed a fair amount of post-buckling capacity.

Specimens B270 had the maximum web height, combined with relatively narrow flanges. Not surprisingly, local buckling was first detected in the web (Fig. 20). The buckling load, as determined from the experimental data in Fig. 18(b), was 10.9 kNm for a single channel. Some minor participation of the distortional mode was observed shortly before the peak load. A highly unstable post-peak response was obtained. Fig. 21 shows various stages of deformation of specimen B270-2.

In specimens C180 local bucking mainly manifested itself in the top flanges, which comprised the most slender part of the cross-section. At higher loads, participation of the web in the local buckling pattern also became noticeable. Simultaneous distortional buckling was observed, as seen in Fig. 22. The experimentally determined buckling moment (Fig. 18(c)) was 6.07 kNm, which agreed well with the calculated value of 6.31 kNm (Table 8). Fig. 23 shows specimen C180-2 at various stages of increasing deformation.

All test specimens showed an anti-symmetric distortionally buckled shape, in which the lip of one channel moved upward while the lip of the other channel moved downward, as a result of contact between the webs. Past the peak load the buckling deformations localized in all specimens, forming an anti-symmetric yield line pattern in both flanges of the back-to-back channels (Fig. 24).

7 Comparison with various design methodologies

7.1 Comparison with EN1993-1-3 (2006)

Table 9 presents a comparison between the experimentally measured ultimate capacities M_u and the capacities M_{EC3} predicted by EN1993-1-3. The Eurocode provisions require iterative calculations, both because the location of the neutral axis of the effective cross-section is initially unknown, and because of the iterative nature of the distortional buckling calculations. Full iterations to convergence were carried out, although not strictly prescribed by the Eurocode. The measured dimensions (Tables 1-3) and the material properties obtained from the coupon tests (Table 5) were used in the calculations.

Table 9 shows that EN1993-1-3 provided rather accurate predictions for the channels under consideration. The predictions are generally safe, although slightly conservative for specimens A230. The average ratio of M_{EC3}/M_u is 0.95 with a standard deviation of 0.04.

7.2 Comparison with various DSM approaches

The test results were further used to assess the accuracy of the current DSM provisions, as well as to evaluate various DSM-based alternative design rules previously proposed in the literature with the specific purpose of accounting for local-distortional interaction. All calculations were again based on the measured cross-sectional dimensions of the channels and the material properties obtained from the coupon tests.

The current AISI (2016) DSM equations for the local and distortional strength of beams, evaluated in the case where lateral-torsional buckling is not an issue (i.e. the lateral-torsional buckling moment capacity $M_{ne} = M_y$) are as follows:

$$M_{nl} = \begin{cases} M_y + \left(1 - C_{yl}^{-2}\right)(M_P - M_Y) & for\ \lambda_l \leq 0.776 \\ \left[1 - 0.15\left(\dfrac{M_{crl}}{M_y}\right)^{0.4}\right]\left(\dfrac{M_{crl}}{M_y}\right)^{0.4} M_y & for\ \lambda_l > 0.776 \end{cases} \tag{6}$$

$$M_{nd} = \begin{cases} M_y + \left(1 - C_{yd}^{-2}\right)(M_P - M_Y) & for\ \lambda_d \leq 0.673 \\ \left[1 - 0.22\left(\dfrac{M_{crd}}{M_y}\right)^{0.5}\right]\left(\dfrac{M_{crd}}{M_y}\right)^{0.5} M_y & for\ \lambda_d > 0.763 \end{cases} \tag{7}$$

In the above equations, $\lambda_l = \sqrt{M_y/M_{crl}}$ and $\lambda_d = \sqrt{M_y/M_{crd}}$, where M_{crl} and M_{crd} are the elastic local

and distortional buckling moments, respectively. C_{yl} and C_{yd} depend on λ_l and λ_d, respectively, and

determine the amount of inelastic reserve capacity present in stocky sections. M_{nl} and M_{nd} are the

capacities in local and distortional buckling, respectively, and they are listed for the tested channels in Table

10.

The NLD and the NDL approaches, originally proposed by Schafer (2002) and Silvestre et al. (2012) to

account for local-distortional buckling interaction, take the above Eqs. (6-7) as a starting point. In the NLD

approach, the bending capacity accounting for local-distortional interaction M_{nld} is computed using Eq. (6),

but with M_y replaced by the capacity in pure distortional buckling M_{nd}, itself obtained from Eq. (7). Similarly,

in the NDL approach the bending capacity M_{ndl} is calculated using Eq. (7), but this time M_y is replaced by M_{nl},

obtained from Eq. (6). The predictions using the NLD and NDL approaches are also listed in Table 10 for the

tested geometries.

The approaches proposed by Martins et al. (2017c) for beams subject to local-distortional interaction were

also evaluated. They are, in principle, identical to the NLD and NDL approaches previously described, but the

original DSM strength curve for distortional buckling given by Eq (7) is replaced by the distortional strength

curves proposed by Martins et al. (2017d). These curves were developed based on numerical simulations of

beams with different cross-sectional geometries, subject to a constant moment and considering two

variations of simply supported boundary conditions: SCA and SCB. Both conditions allow rotations about the

major and minor axes of the cross-section and restrain twist. However, in case SCA the warping

displacements and the local displacements and rotations in the end sections are free to occur, while in case

SCB these are restrained. For lipped channels bent about their major axis the DSM distortional strength

curves for end conditions SCA and SCB are given by:

$$M_{ndSCA} = \begin{cases} M_y + \left(1 - C_{yd}^{-2}\right)(M_P - M_Y) & for\ \lambda_d \leq 0.673 \\ \left[1 - 0.25\lambda_d^{-1.75}\right]\lambda_d^{-1.75}M_y & for\ \lambda_d > 0.673 \end{cases} \tag{8}$$

$$M_{ndSCB} = \begin{cases} M_y + \left(1 - C_{yd}^{-2}\right)(M_P - M_Y) & for\ \lambda_d \leq 0.673 \\ \left[1 - 0.23\lambda_d^{-1.55}\right]\lambda_d^{-1.45}M_y & for\ \lambda_d > 0.763 \end{cases} \tag{9}$$

By combining either one of these distortional curves with the NLD or NDL approaches, four different moment predictions are obtained (M_{nldSCA}, M_{nldSCB}, M_{ndlSCA} and M_{ndlSCB}). They are listed in Table 10 for the tested geometries.

The final DSM design approach considered in this study was proposed by Anbarasu (2016) and was developed based on numerical simulations of lipped channel beams for which the elastic local and distortional buckling moments were almost equal. In this method a single DSM-style equation is provided to calculate the capacity M_{Anb}:

$$M_{Anb.} = \begin{cases} M_y & for\ \lambda_d \leq 0.610 \\ \left[0.472\left(\dfrac{M_{crd}}{M_y}\right)^{0.735}\right]M_y & for\ \lambda_d > 0.610 \end{cases} \tag{10}$$

The predicted capacities M_{Anb} for all test specimens are listed in Table 10.

Table 11 presents the ratios of the ultimate capacities obtained using the various prediction methods to the capacities obtained from the experiments. It can be concluded that the current AISI DSM philosophy of obtaining the cross-sectional bending capacity as the minimum value of M_{nl} and M_{nd} leads to reasonably accurate results for all the tested geometries. The results are most conservative for the B270 specimens, with an average ratio of the predicted capacity to the measured capacity of 0.86. This might be explained by the relatively high ratio of M_{crd} to M_{crl} (= 1.62) and the fact that local buckling manifested itself mainly in the web rather than the flange, limiting the effects of the local-distortional interaction. The DSM predictions are least conservative for specimens C180, with an average ratio of the predicted capacity to the measured value of 1.02. These specimens possessed the widest flanges and exhibited an M_{crd}/M_{crl} ratio of 0.84. Over the whole range of test specimens, the average ratio of the DSM predicted capacity to the measured one was 0.95 with a standard deviation of 0.063. A comparison of the test results with the current DSM design rules is graphically presented in Fig. 25.

The alternative DSM formulations based on the NLD and NDL approaches resulted in rather conservative predictions for the tested geometries. The ratio of the predicted capacity to the measured one was typically around 0.7, irrespective of the geometry or the employed method.

Out of the various approaches considered, the method proposed by Anbarasu (2016) resulted in the most conservative predictions, irrespective of whether the local and distortional stresses were close or not. None of the ratios of the predicted capacity to the measured capacity were larger than 0.5.

It should be noted that the predictions of the elastic distortional buckling moments in Table 11 were carried out on the basis of the half-wavelengths listed in Table 4. In other words, the distortional moment corresponded to the relevant minimum in the signature curve. On the other hand, the constant moment span in the experimental set-up had a length of 1200 mm, allowing two distortional half-waves of 600 mm length. This only resulted in a slight reduction of the half-wave length compared to the natural half-wavelength for specimens A230 and B270, with negligible repercussions for the predictions in Table 11, due to the relative flatness of the signature curve around the distortional minimum. For specimens C180, with a slightly longer distortional half-wavelength of 775 mm, however, determining M_{nd} based on L_{crd} = 600 mm increased the value of M_{nd} by a modest 4-5%. The predicted moment capacities based on these updated values of M_{nd} are summarized in Table 12. The table reinforces the earlier conclusion that the current DSM equations are slightly on the unsafe side for specimens C180.

It should be noted that, as previously pointed out by Martins et al. (2017c), the boundary conditions at the ends of the constant moment span in a four-point bending test do not allow free warping. Rather, the warping displacements are continuous into the adjacent shear spans which experience a linearly decreasing moment. It has been shown through numerical simulations that this may lead to a moderate increase in the distortional post-buckling capacity compared to the case where warping is free. However, in this context it should be mentioned that the DSM strength curves themselves were also calibrated mostly with the help of experimental data resulting from four-point bending tests and that, consequently, a direct comparison between the test results and the DSM design rules is appropriate. On the other hand, the NLD/NDL SCA

approaches considered above were calibrated based on numerical simulations with boundary conditions including free warping, which may to some extent explain why they were found to be more conservative.

8 Conclusions

A total of six beams, assembled from lipped channels in a back-to-back configuration, were tested to investigate the interaction between local and distortional buckling. Three different cross-sectional geometries were considered with progressively deeper webs and narrower flanges. The specimens were tested in a four-point bending configuration with simply supported boundary conditions, while being laterally braced at the loading points. The geometric imperfections were recorded before the test using a specially designed set-up with a laser sensor. Coupons extracted from both the web and the web-flange junction of each cross-section type were also tested to determine the material properties.

Simultaneous local and distortional buckling was observed in all test specimens, either as 'true interaction' or secondary bifurcation. No lateral-torsional buckling was observed. The critical buckling loads agreed well with the calculated elastic values.

The cross-sectional bending capacities obtained from the test results were compared to the EN1993-1-3 (2006) predictions and these predictions were found to be safe and reasonably accurate for the considered geometries. The average ratio of the predicted capacity to the measured capacity was 0.95 with a standard deviation of 0.04. The current AISI (2016) DSM equations were also evaluated and were found to yield safe predictions, with an average ratio of the predicted capacity to the measured value of 0.95 and a standard deviation of 0.06. This might indicate that the erosion of the ultimate capacity due to local-distortional interaction remained fairly moderate in the tested geometries. Alternative DSM formulations based on the NLD and NDL concepts gave rather conservative predictions of the specimen capacities.

Acknowledgments

References

American Iron and Steel Institute AISI (2016), North American specification (NAS) for the design of cold-formed steel structural members (AISI-S100-16), Washington DC.

Anbarasu, M. (2016), "Local-distortional buckling interaction on cold-formed steel lipped channel beams", *Thin-Walled Structures*, 98, 351-359.

Becque, J. (2014), "Local-overall interaction buckling of inelastic columns: A numerical study of the inelastic Van der Neut column", *Thin-Walled Structures*, 81, 101-107.

Bijlaard, P.P., and Fisher, G.P. (1953), "Column Strength of H-Sections and Square Tubes in Post Buckling Range of Component Plates", *TN 2994, NACA*, Washington, D.C.

British Standard (2008), Specification for surface plates BS817.

CEN (2006), Eurocode 3: Design of Steel Structures, part 1-5: Plated structural elements. Brussels: European Comittee for Standardization.

CEN (2009). Eurocode 3: design of steel structures, part 1.3: general rules—supplementary rules for cold formed members and sheeting. Brussels: European Comittee for Standardization.

Dinis, P. B. and Camotim, D. (2010), "Local/distortional mode interaction in cold-formed steel lipped channel beams", *Thin-Walled Structures*, 48, 771-785.

Dinis, P. B. and Camotim, D. (2015), "Cold-formed steel columns undergoing local-distortional coupling: Behaviour and direct strength prediction against interactive failure", *Computers and Structures*, 147, 181-208.

Dinis, P. B., Young, B. and Camotim, D. (2014), "Local-distortional interaction in cold-formed steel rack-section columns", *Thin-Walled Structures*, 81, 185-194.

Dubina D, Ungureanu V. (2002), "Effect of imperfections on numerical simulation of instability behaviour of cold-formed steel members", *Thin-Walled Structures*, 40, 239-62.

Fiorino, L., Iuorio, O. and Landolfo, R. (2014), "Designing CFS structures: The new school bfs in naples", *Thin Walled Structures*, 78, 37-47.

Graves Smith, T.R. (1969) "The Ultimate Strength of Locally Buckled Columns of Arbitrary Length", Proc., Symposium on Thin-Walled Structures, Swansea, 1967, *Thin-Walled Structures*, Crosby-Lockwood, eds. K.C. Rockey and H.V. Hill, 35-60.

ISO E. 6892-1. Metallic materials-Tensile testing-Part 1: Method of test at room temperature. International Organization for Standardization 2009.

Kwon, Y. B. and Hancock, G. J. (1992), T"ests of cold-formed channels with local and distortional buckling", *Journal of Structural Engineering*, 118 (7), 1786-1803.

Kwon, Y. B. and Hancock, G. J (1993), "Post-buckling analysis of thin-walled channel sections undergoing local and distortional buckling", *Computers and Structures*, 49 (3), 507-516.

Kwon, Y. B., Kim, B. S. and Hancock, G. J. (2009), "Compression tests of high strength cold-formed steel channels with buckling interaction", *Journal of Constructional Steel Research*, 65, 278-289.

Laím, L., Rodrigues, J.P.C., and da Silva, L.S. (2013). "Experimental and numerical analysis on the structural behaviour of cold-formed steel beams", *Thin-Walled Structures*, 72, 1-13.

Lim, J. B. P. and Nethercot, D. A. (2003), "Ultimate strength of bolted moment-connections between cold-formed steel members", *Thin Walled Structures*, 41, 1019-1039.

Lim, J. B. P. and Nethercot, D. A. (2004), "Finite element idealization of a cold-formed steel portal frame", *Journal of Structural Engineering*, 130, 78-94.

Martins, A. D., Camotim, D. and Dinis, P. B. (2017a), "Behaviour and DSM design of stiffened lipped channel columns undergoing local-distortional interaction", *Journal of Constructional Steel Research*, 128, 99-118.

Martins, A. D., Camotim, D. and Dinis, P. B. (2017b), "On the direct strength design of cold-formed steel columns failing in local-distortional interactive modes", *Thin-Walled Structures*, 120, 432-445.

Martins, A. D., Camotim, D. and Dinis, P. B. (2017c), "Local-distortional interaction in cold-formed steel beams: Behaviour, strength and DSM design", *Thin-Walled Structures*, 119, 879-901.

Martins, A. D., Dinis, P. B., Camotim, D. and Providencia, P. (2015), "On the relevance of local-distortional interaction effects in the behaviour and design of cold-formed steel columns", *Computers and Structures*, 160, 57-89.

Martins, A. D., Landesmann, A. Camotim, D. and Dinis, P. B. (2017d), "Distortional failure of cold-formed steel beams under uniform bending: Behaviour, strength and DSM design", *Thin-Walled Structures*, 118, 196-213.

Moen, C.D., Schudlich, A., and von der Heyden, A. (2013). "Experiments on cold-formed steel C-section joists with unstiffened web holes." Journal of Structural Engineering, 139(5), 695-704.

Schafer, B. W. (2002), "Local, distortional and Euler buckling of thin-walled columns", *Journal of Structural Engineering*, 128, 289-299.

Schafer, B. W. (2011), "Cold-formed steel structures around the world - A review of recent advances in applications, analysis and design", Steel Construction ,4, 3, 141-149.

Schafer, B.W., and Adany, S. (2006). "Buckling analysis of cold-formed steel members using CUFSM: conventional and constrained finite strip methods", Proceedings of the eighteenth international specialty conference on cold-formed steel structures, Orlando, USA.

Silvestre, N., Camotim, D. and Dinis, P. B. (2009), "Direct strength prediction of lipped channel columns experiencing local-plate/distortional interaction", *Advanced Steel Construction*, 5 (1), 49-71.

Silvestre, N., Camotim, D. and Dinis, P. B. (2012), "Post-buckling behaviour and direct strength design of lipped channel columns experiencing local/distortional interaction", *Journal of Constructional Steel Research*, 73, 12-30.

Standards Australia (2005), Cold-formed steel structures AS/NZS 4600:2005, Sydney, NSW, Australia.

van der Neut, A. (1969), "The interaction of Local Buckling and Column Failure of Thin-walled Compression Members", *Proceedings of the 12th International Congress on Applied Mechanics*, 389-399.

Wang, L., and Young , B. (2015). "Beam tests of cold-formed steel built-up sections with web perforations", *Journal of Constructional Steel Research*, 115, 18–33.

Wang, L., and Young , B. (2016a). "Behavior of cold-formed steel built-up sections with intermediate stiffeners under bending. I: Tests and numerical validation", *Journal of Structural Engineering*, 142(3).

Wang, L., and Young , B. (2016b). "Behavior of cold-formed steel built-up sections with intermediate stiffeners under bending. II: Parametric study and design", *Journal of Structural Engineering*, 142(3).

Yang, D. and Hancock, G. J. (2004), "Compression tests of high strength steel channel columns with interaction between local and distortional buckling", *Journal of Structural Engineering*, 130, 1954-1963.

Yap, D. C. Y. and Hancock, G. J. (2008), "Experimental study of complex high-strength cold-formed cross-shaped steel section", *Journal of Structural Engineering*, 134 (8), 1322-1333.

Young, B., Silvestre, N. and Camotim, D. (2013), "Cold-formed steel lipped channel columns influenced by local-distortional interaction: Strength and DSM design", *Journal of Structural Engineering*, 139 (6), 1059-1074.

Zhou, X.-H. and Shi, Y. (2011). "Flexural strength evaluation for cold-formed steel lip-reinforced built-up I-beams", *Advances in Structural Engineering,* 14(4),*597-611.*

Table 1. Measured dimensions of specimens with cross-section A

Specimen	Channel	r (mm)	t (mm)	h (mm)	b_1 (mm)	c_1 (mm)	b_2 (mm)	c_2 (mm)	I_y (mm^4)
A230-1	a	3.9	1.563	230.43	75.36	17.44	75.35	16.81	4894400
	b	4.3	1.551	230.35	75.33	17.44	75.33	16.86	4844375
A230-2	a	4.1	1.557	230.52	75.35	16.64	75.35	17.39	4863925
	b	3.7	1.564	230.48	74.90	16.09	74.90	17.25	4889340
Average		4.0	1.559	230.45	75.24	16.90	75.23	17.08	4873010
St. Dev.		0.15	0.01	0.07	0.22	0.66	0.22	0.29	23286

Table 2. Measured dimensions of specimens with cross-section B

Specimen	Channel	r (mm)	t (mm)	h (mm)	b_1 (mm)	c_1 (mm)	b_2 (mm)	c_2 (mm)	I_y (mm^4)
B270-1	a	4.1	1.561	269.49	50.19	24.70	50.10	23.79	5983335
	b	4.0	1.565	270.59	51.33	23.24	49.71	23.47	5998320
B270-2	a	4.2	1.555	270.43	50.95	23.01	49.91	23.50	5955795
	b	4.1	1.546	270.55	51.34	23.29	50.25	22.84	5940270
Average		4.1	1.557	270.30	51.00	23.60	50.00	23.40	5969430
St. Dev.		0.08	0.01	0.52	0.54	0.77	0.23	0.40	26231

Table 3. Measured dimensions of specimens with cross-section C

Specimen	Channel	r (mm)	t (mm)	h (mm)	b_1 (mm)	c_1 (mm)	b_2 (mm)	c_2 (mm)	I_y (mm^4)
C180-1	A	4.1	1.554	180.30	100.41	17.31	100.33	17.06	3250607
	B	3.9	1.567	180.20	100.38	17.53	100.14	16.80	3288756
C180-2	A	3.9	1.559	180.52	100.41	17.46	100.33	17.28	3287688
	B	4.2	1.554	180.41	100.43	17.34	100.32	16.75	3250202
Average		4.0	1.559	180.36	100.41	17.41	100.28	16.97	3269313
St. Dev.		0.15	0.01	0.14	0.02	0.10	0.09	0.25	21839

Table 4. Elastic local and distortional buckling moments

Section	M_{crl} (kNm)	M_{crd} (kNm)	L_{crl} (mm)	L_{crd} (mm)	M_y (kNm)	M_{crd}/M_{crl} -	M_{crl}/M_y -	M_{crd}/M_y -
A230	9.91	9.89	130	670	17.6	1.00	0.56	0.56
B270	8.31	13.48	140	620	18.8	1.62	0.44	0.72
C180	7.58	6.37	100	775	16.0	0.84	0.47	0.40

Table 5. Tensile properties of flat and corner coupons

Section	Type	E (GPa)	f_y (MPa)	σ_u (MPa)	ε_f (%)
A230	flat	196	416	511	18
	corner	218	516	575	6
B270	flat	199	424	517	17
	corner	208	508	560	(4)
C180	flat	200	427	521	18
	corner	209	514	576	7

Table 6. Maximum amplitudes of local and distortional imperfections

Specimen	Local (*mm*)	Distortional (*mm*)
A230-1a	0.33	0.38
A230-1b	0.36	0.34
A230-2a	0.33	0.26
A230-2b	0.29	0.26
B270-1a	0.31	0.17
B270-1b	0.36	0.16
B270-2a	0.41	0.22
B270-2b	0.36	0.21
C180-1a	0.10	0.27
C180-1b	0.10	0.35
C180-2a	0.10	0.31
C180-2b	0.09	0.32

Table 7. Ultimate capacities of test specimens

Specimen	Capacity (kNm)
A230-1	23.72
A230-2	23.79
B270-1	(25.83)
B270-2	28.34
C180-1	17.43
C180-2	17.24

Table 8. Comparison of experimental and calculated critical moments (single channel)

Specimen	Critical moment		Difference
	Experimental	Calculated	
	(kNm)	(kNm)	(%)
A230	9.25	9.89	6.9
B270	10.90	8.31	-23.8
C180	6.07	6.31	4.0

Table 9. Comparison of test results with EN1993-1-3 predictions

	M_u	M_{EC3}	M_{EC3}/M_u
	kNm	kNm	-
A230-1	23.72	21.35	0.90
A230-2	23.79	21.61	0.91
B270-2	28.34	27.91	0.98
C180-1	17.43	16.86	0.97
C180-2	17.24	17.06	0.99
Average			0.95
St. dev.			0.04

Table 10: Predicted ultimate bending capacities

Channel	M_{nl} (kNm)	M_{nd} (kNm)	M_{nld} (kNm)	M_{ndl} (kNm)	M_{nldSCA} (kNm)	M_{nldSCB} (kNm)	M_{ndlSCA} (kNm)	M_{ndlSCB} (kNm)	$M_{Anb.}$ (kNm)	M_u (kNm)
A230-1a	12.51	11.30	9.30	9.13	8.21	8.70	8.40	8.78	5.67	11.86
A230-1b	12.39	11.07	9.15	8.96	8.04	8.53	8.18	8.58	5.51	11.86
A230-2a	12.47	11.11	9.20	9.00	8.08	8.58	8.21	8.61	5.52	11.9
A230-2b	12.58	11.11	9.24	9.02	8.10	8.60	8.19	8.60	5.49	11.9
B270-2a	12.19	13.05	9.63	9.95	8.92	9.26	9.82	9.98	7.08	14.17
B270-2b	12.10	12.98	9.54	9.86	8.83	9.17	9.73	9.89	7.02	14.17
C180-1a	10.64	8.83	7.20	6.94	5.89	6.43	5.87	6.34	3.95	8.72
C180-1b	10.75	8.87	7.28	7.00	5.96	6.51	5.92	6.40	3.97	8.72
C180-2a	10.67	8.81	7.21	6.94	5.89	6.44	5.85	6.33	3.93	8.62
C180-2b	10.60	8.73	7.14	6.86	5.81	6.36	5.77	6.26	3.88	8.62

Table 11: Ratios of predicted bending capacities to test results

Channel	M_{nl}/M_u	M_{nd}/M_u	M_{nld}/M_u	M_{ndl}/M_u	M_{nldSCA}/M_u	M_{nldSCB}/M_u	M_{ndlSCA}/M_u	M_{ndlSCB}/M_u	$M_{Anb.}/M_u$
	(-)	(-)	(-)	(-)	(-)	(-)	(-)	(-)	(-)
A230-1a	1.055	0.953	0.784	0.770	0.692	0.733	0.708	0.740	0.478
A230-1b	1.044	0.934	0.771	0.755	0.678	0.719	0.690	0.723	0.464
A230-2a	1.048	0.934	0.773	0.756	0.679	0.721	0.690	0.724	0.464
A230-2b	1.057	0.933	0.777	0.758	0.680	0.723	0.688	0.723	0.462
B270-2a	0.860	0.921	0.680	0.702	0.629	0.654	0.693	0.704	0.500
B270-2b	0.854	0.916	0.674	0.696	0.623	0.647	0.687	0.698	0.496
C180-1a	1.220	1.012	0.826	0.795	0.675	0.737	0.673	0.727	0.453
C180-1b	1.232	1.017	0.835	0.803	0.683	0.746	0.679	0.734	0.456
C180-2a	1.238	1.022	0.837	0.805	0.683	0.747	0.679	0.735	0.456
C180-2b	1.230	1.013	0.828	0.796	0.674	0.738	0.670	0.726	0.450
Avg. A230	1.051	0.938	0.776	0.760	0.682	0.724	0.694	0.727	0.478
Avg. B270	0.857	0.918	0.677	0.699	0.626	0.651	0.690	0.701	0.464
Avg. C180	1.230	1.016	0.831	0.800	0.679	0.742	0.675	0.730	0.464

Table 12: Predicted moment capacities for C180 specimens with L_{crd} = 600 mm

Channel	M_{nl}/M_u	M_{nd}/M_u	M_{nld}/M_u	M_{ndl}/M_u	M_{nldSCA}/M_u	M_{nldSCB}/M_u	M_{ndlSCA}/M_u	M_{ndlSCB}/M_u	$M_{Anb.}/M_u$
	(-)	(-)	(-)	(-)	(-)	(-)	(-)	(-)	(-)
C180-1a	1.220	1.061	0.852	0.832	0.715	0.773	0.728	0.776	0.492
C180-1b	1.232	1.062	0.859	0.836	0.720	0.779	0.729	0.778	0.492
C180-2a	1.238	1.067	0.861	0.838	0.720	0.780	0.730	0.780	0.493
C180-2b	1.229	1.056	0.852	0.828	0.710	0.770	0.719	0.769	0.485
Avg. C180	1.230	1.061	0.856	0.834	0.716	0.775	0.726	0.776	0.490
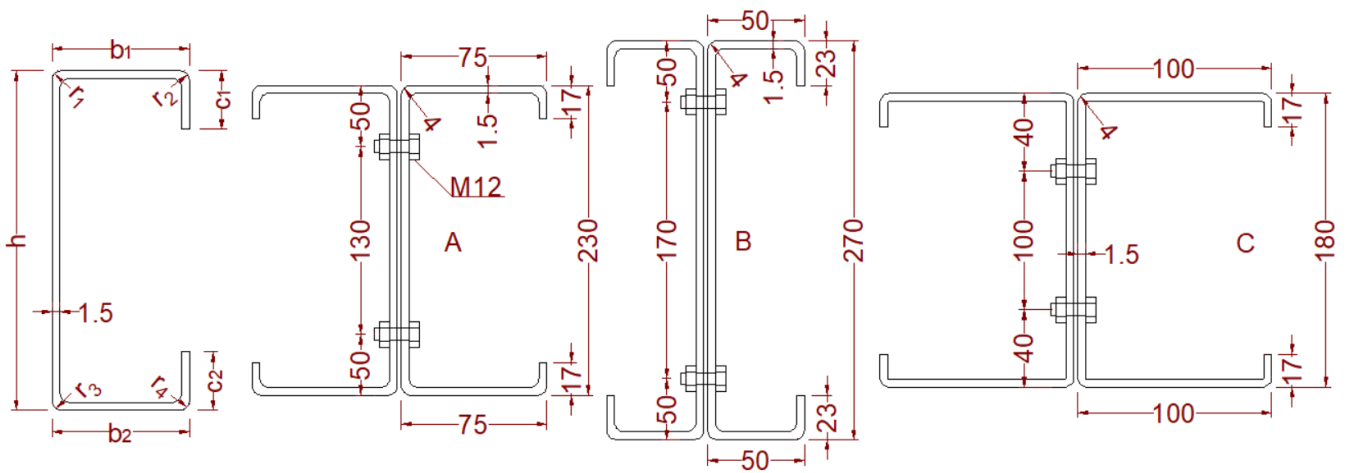
Fig.1: Symbol definitions and nominal cross-sectional dimensions
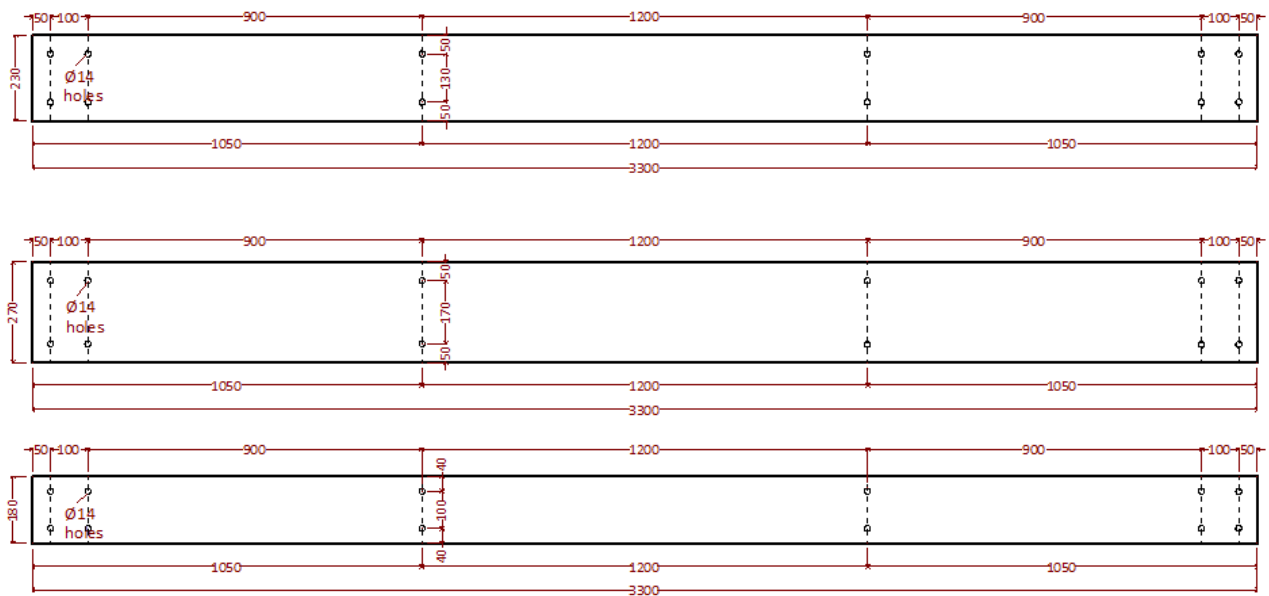
Fig.2: Bolt hole arrangements
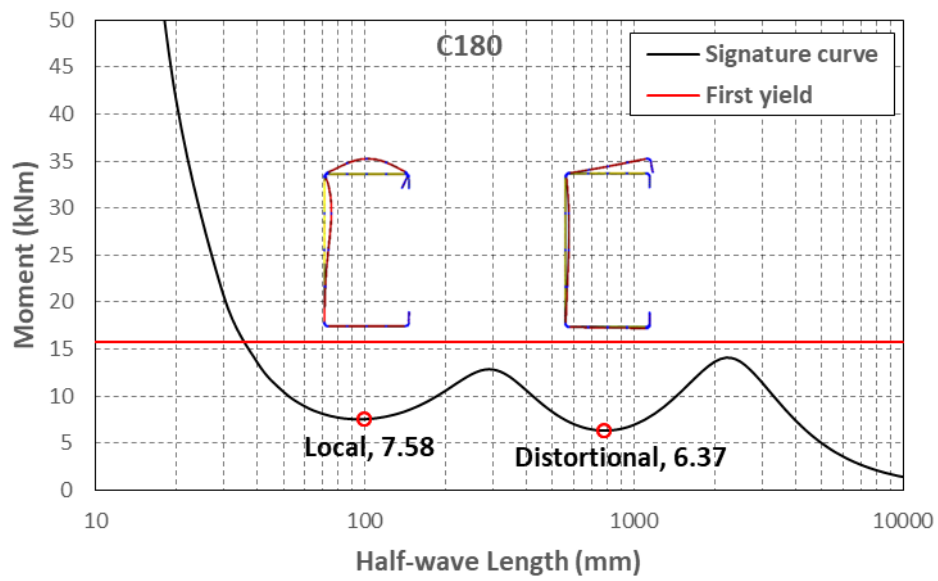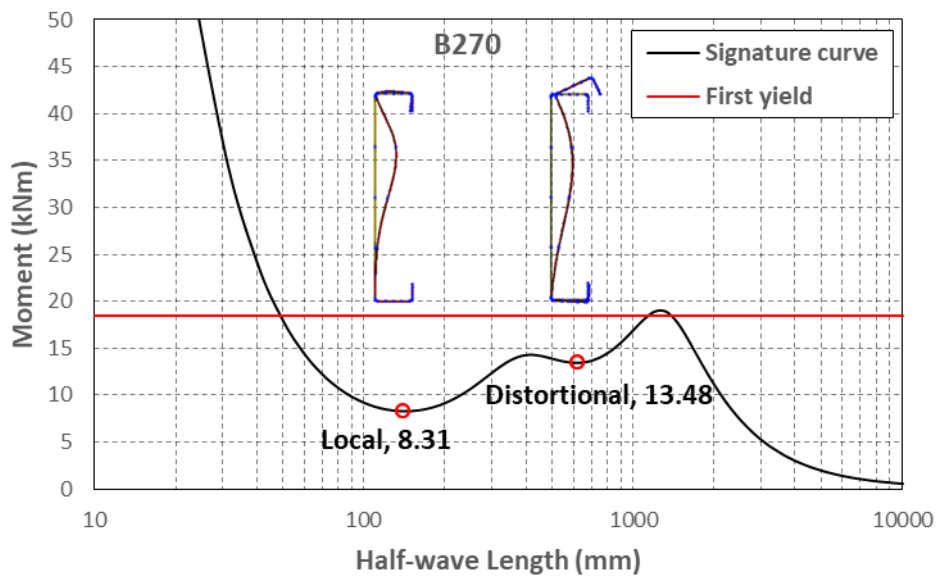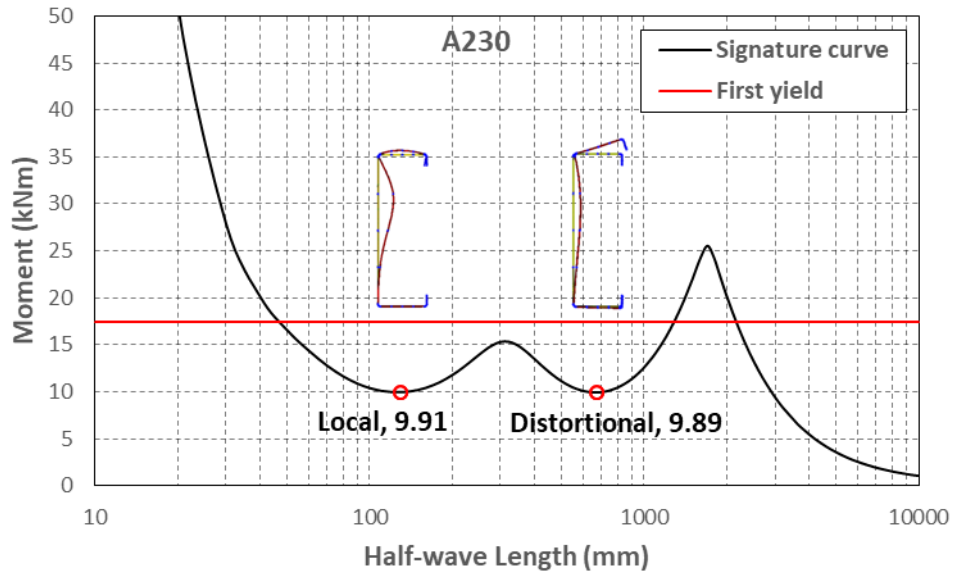
Fig.3: Signature curves obtained from CUFSM for cross-sections A, B and C (individual channels)
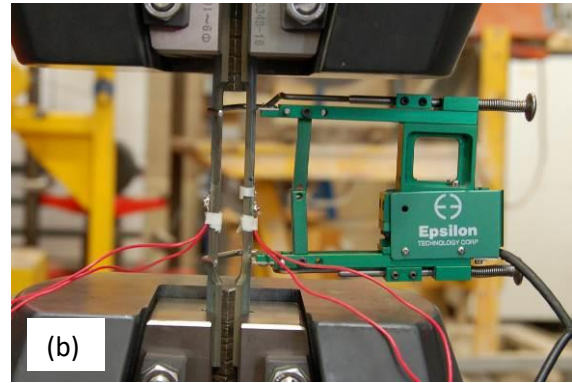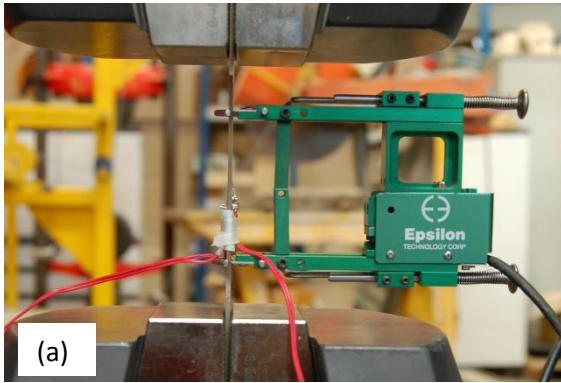
Fig.4: Tensile material tests with: (a) flat coupons (b) corner coupons
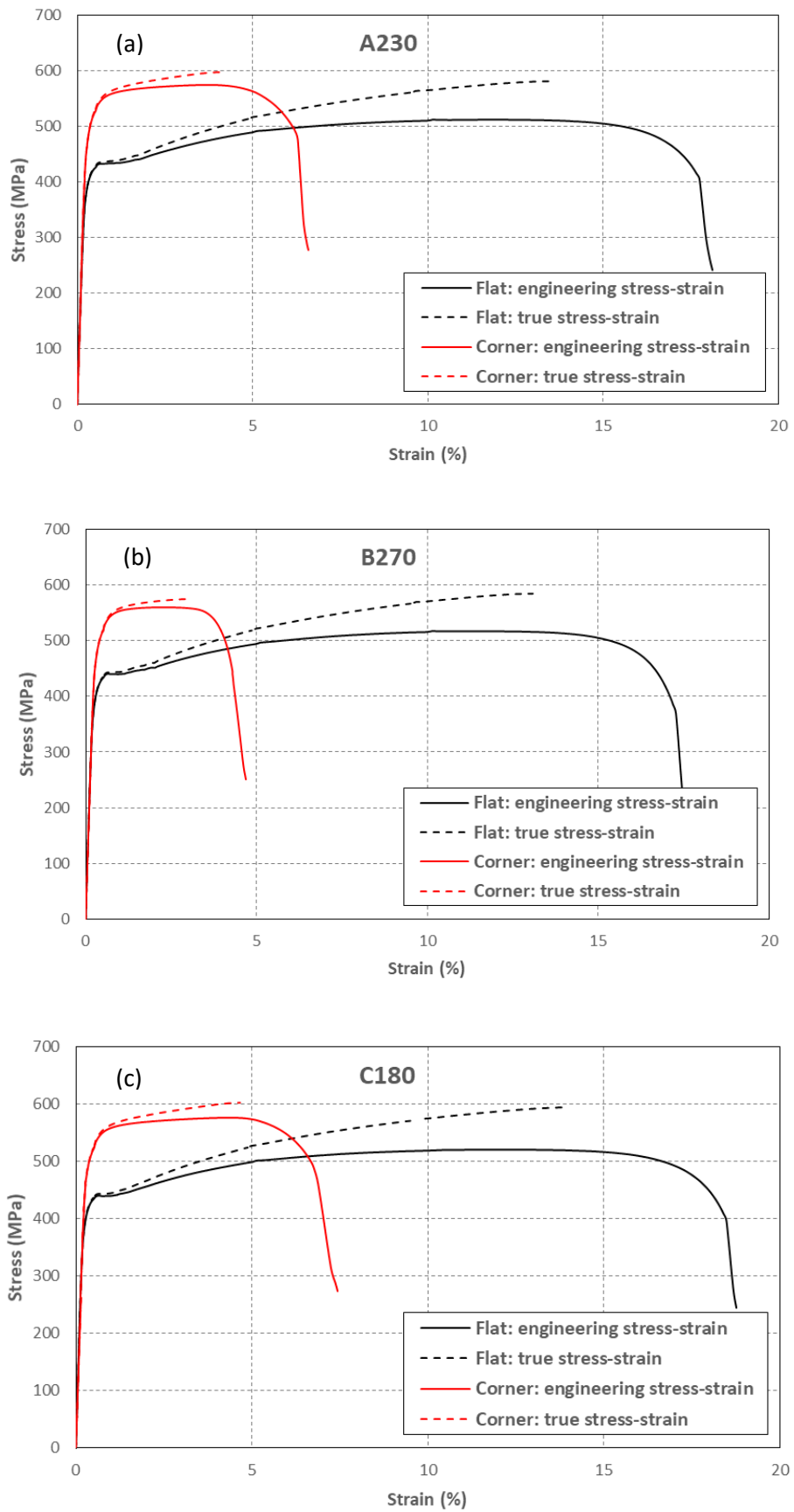
Fig. 5: Stress–strain curves of the flat and corner coupons: a. A230, b. B270, and c. C180 specimens

Fig.6 Imperfection measurement set-up
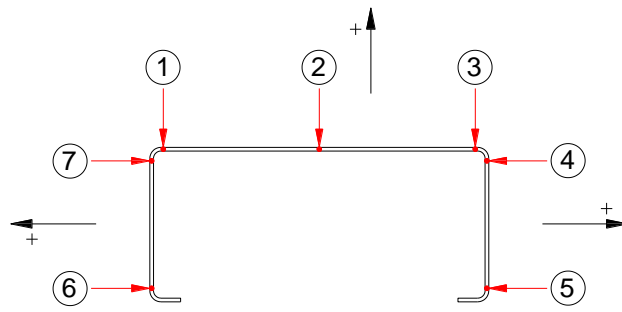
Fig. 7: Locations of the imperfection measurements and sign convention
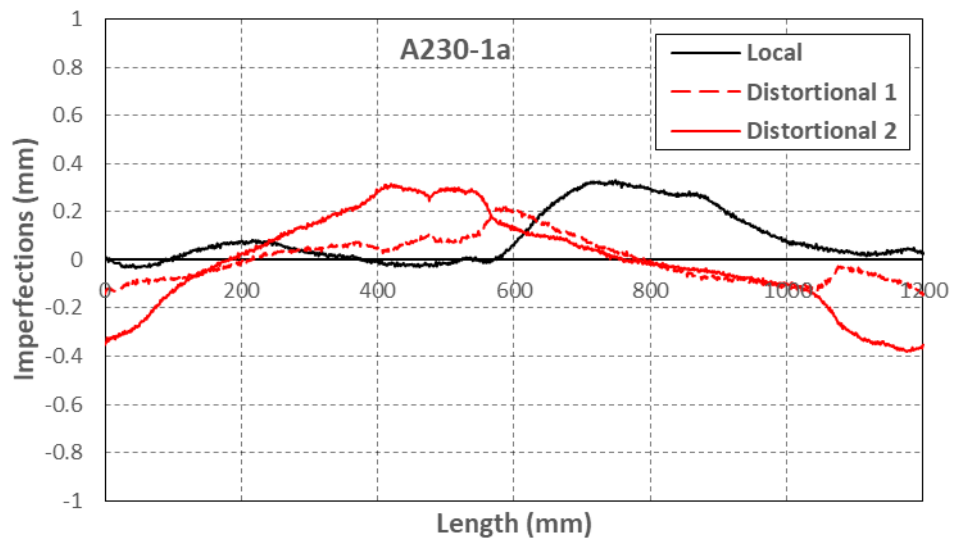
Fig. 8: Local and distortional imperfections of channel A230-1a
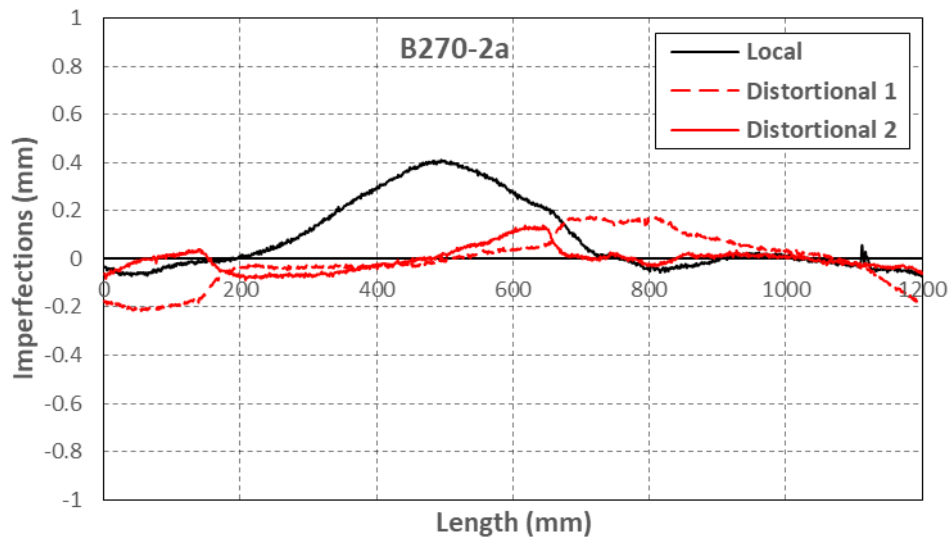
Fig. 9: Local and distortional imperfections of channel B270-2a
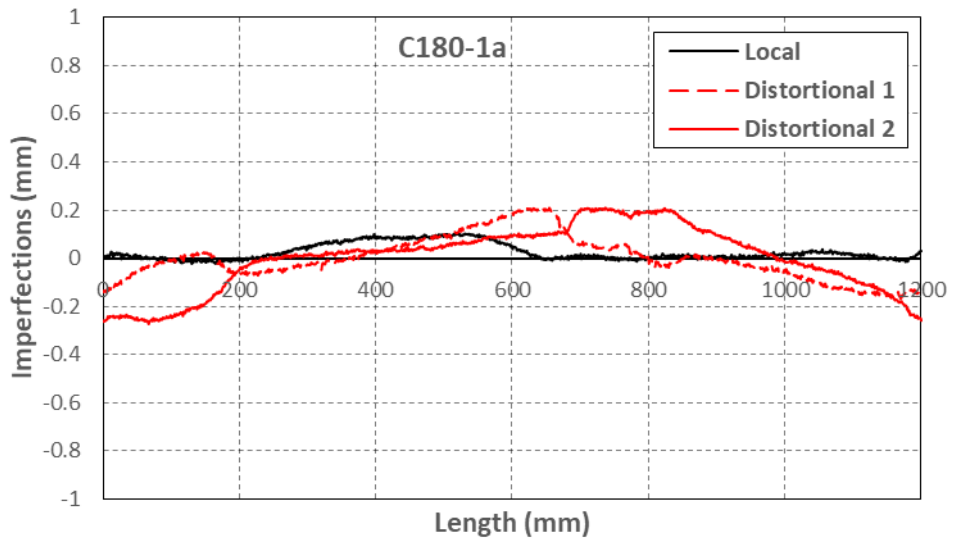
Fig. 10: Local and distortional imperfections of channel C180-1a
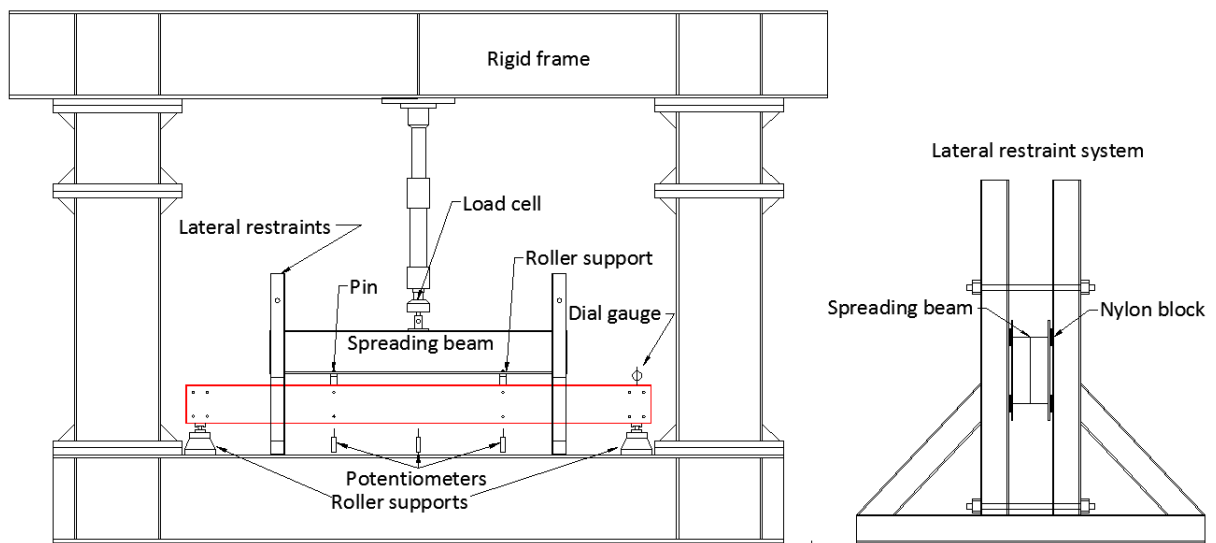
Fig.11: Schematic view of: (a) experimental set-up (b) lateral support system
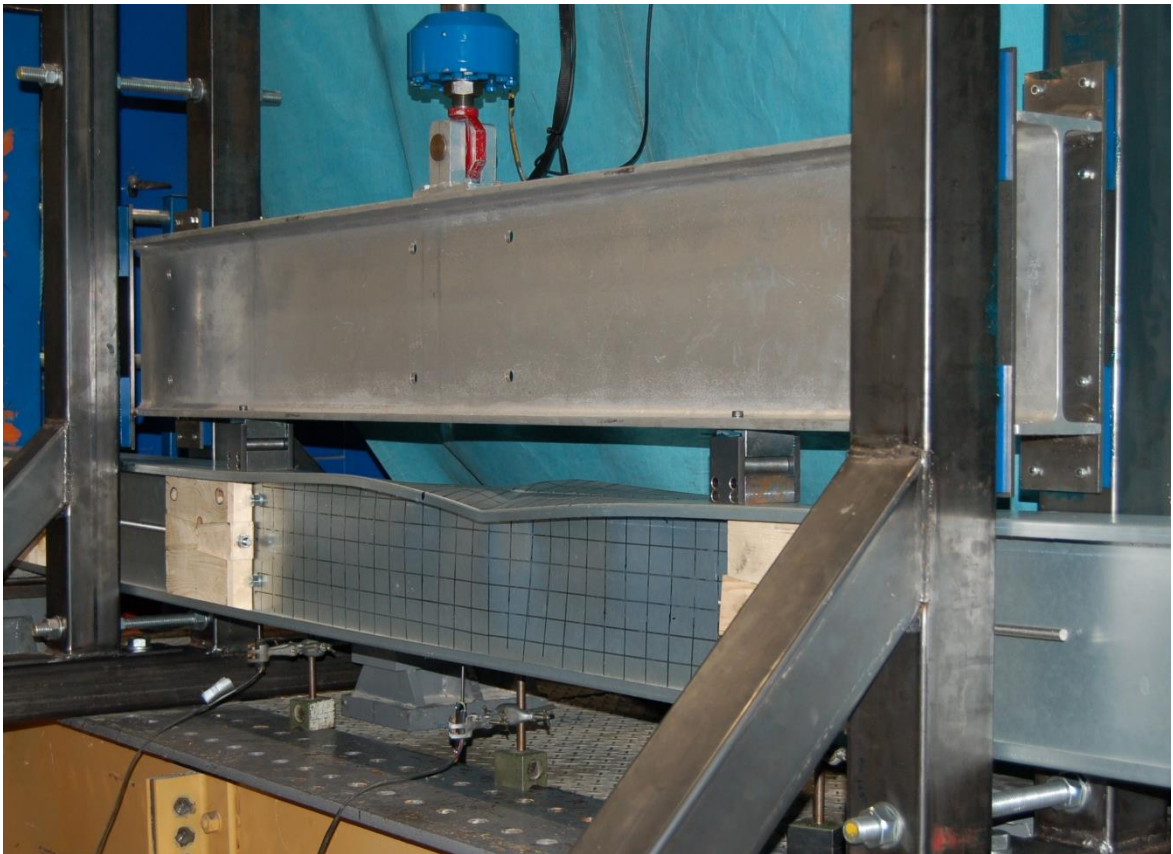
Fig. 12: Test set-up, showing spreader beam supports
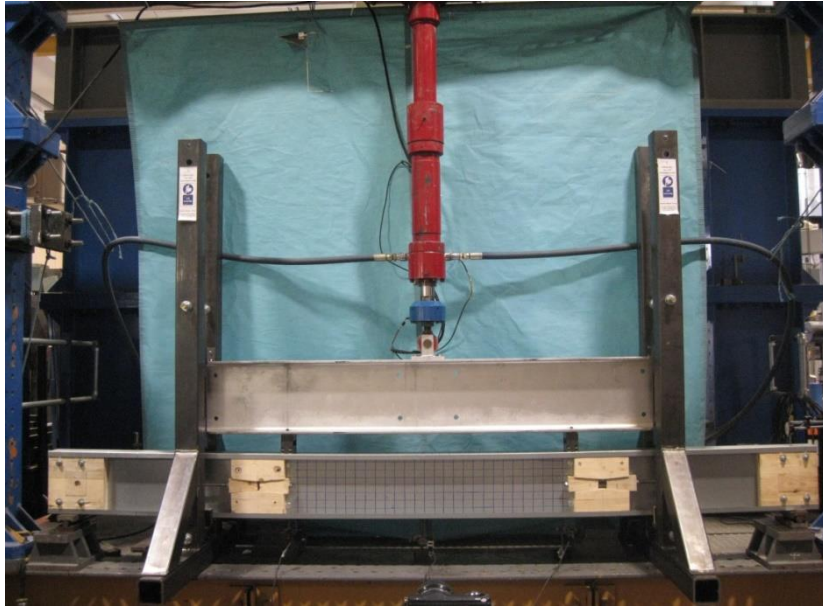
Fig.13: Full view of four-point bending test set-up
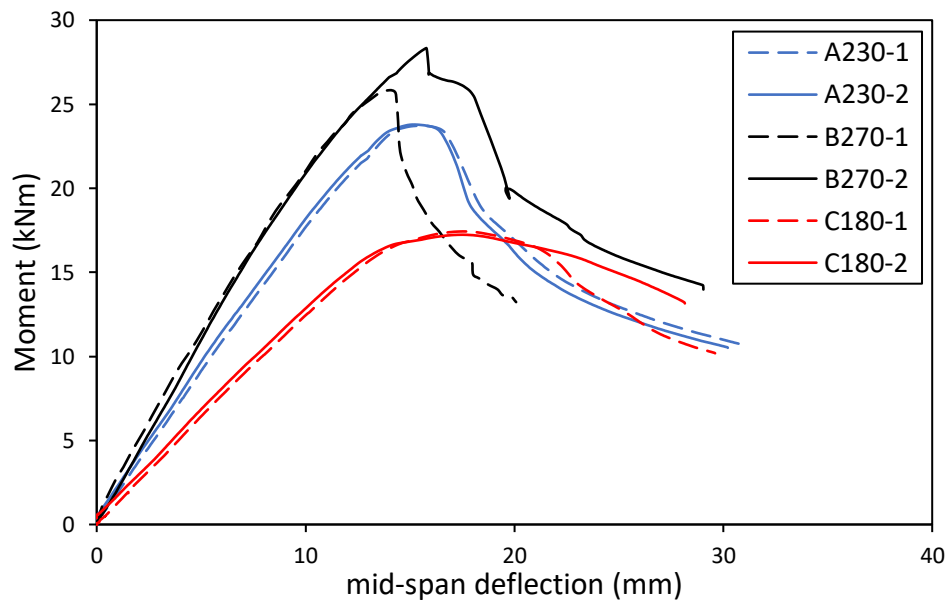
Fig. 14: Moment vs mid-span deflection for all beams
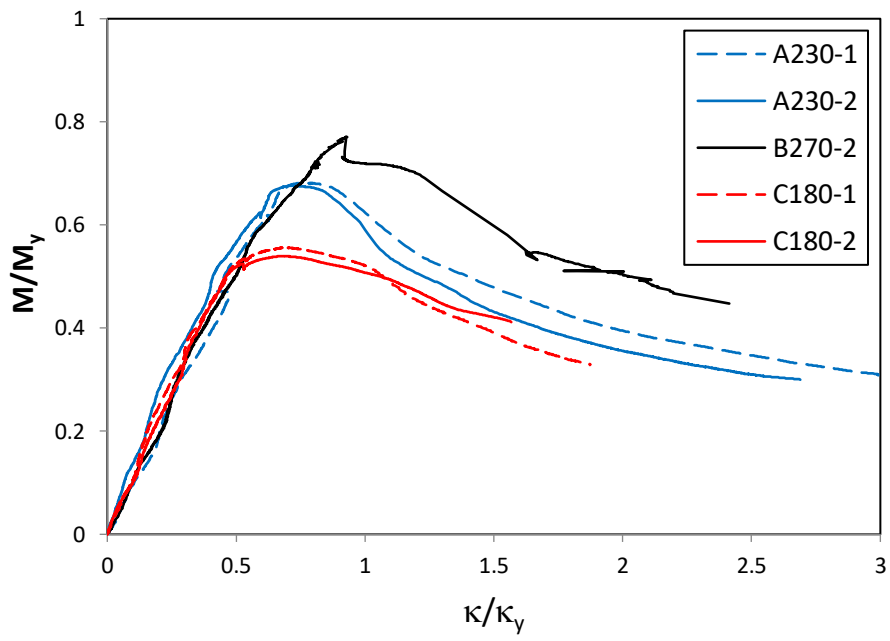
Fig.15: Moment-curvature diagrams
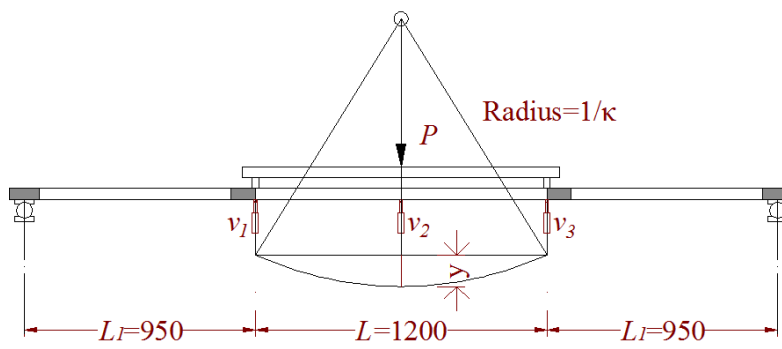
Fig. 16: Calculation of curvature using potentiometer measurements
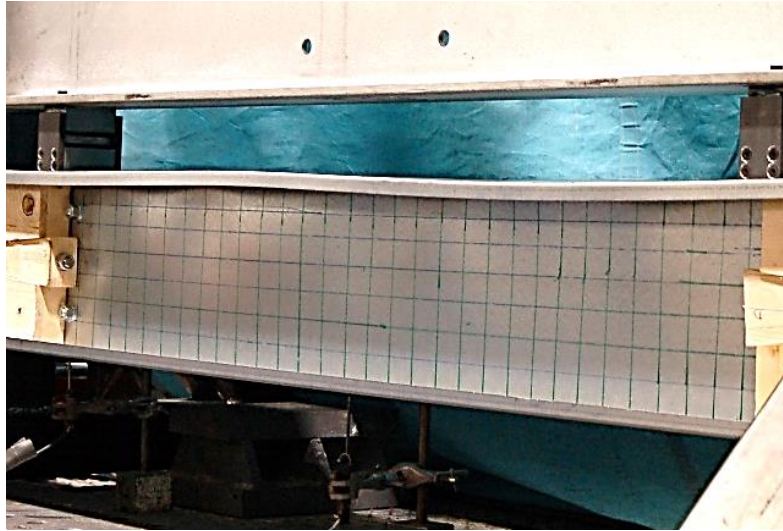
Fig. 17: Buckling pattern in specimen A230-1
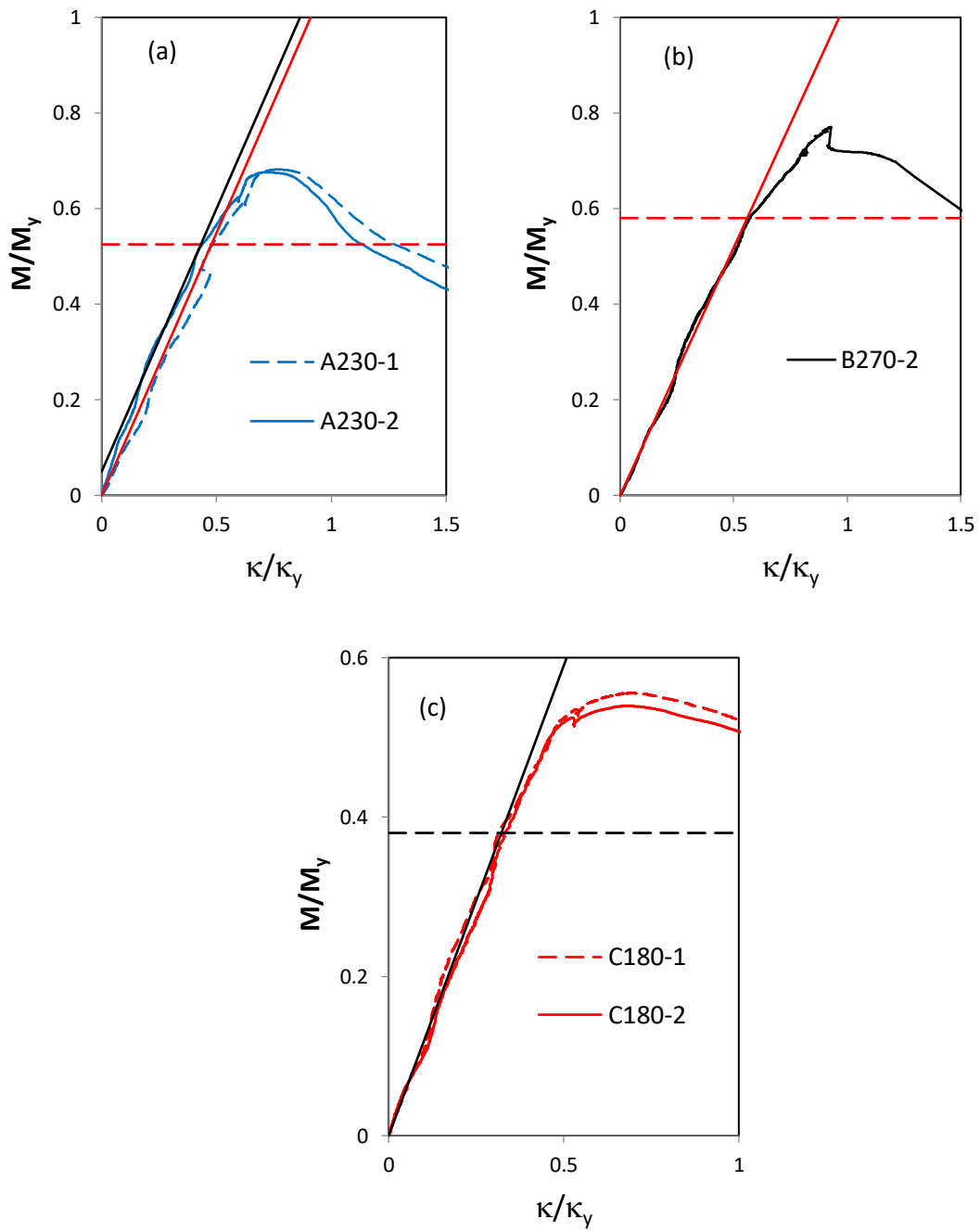
Fig. 18: Determination of the buckling load for: (a) A230 specimens, (b) B270 specimen and (c) C180 specimens
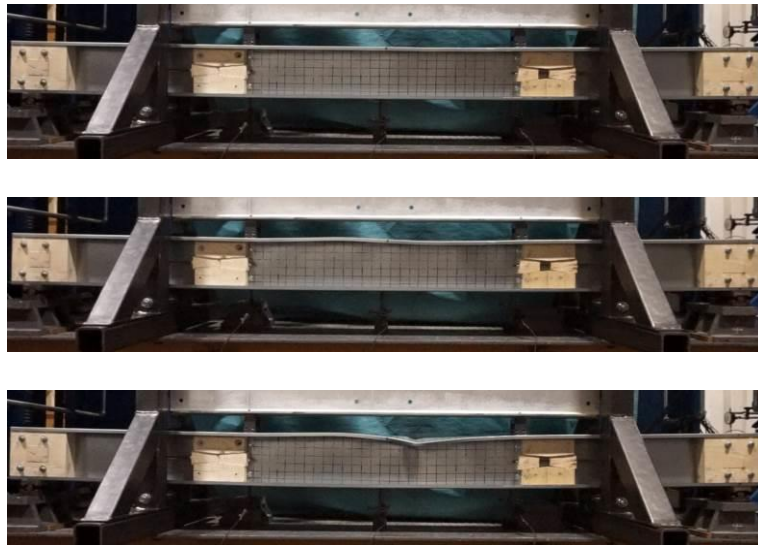
Fig. 19: Progressive deformations of beam A230-2
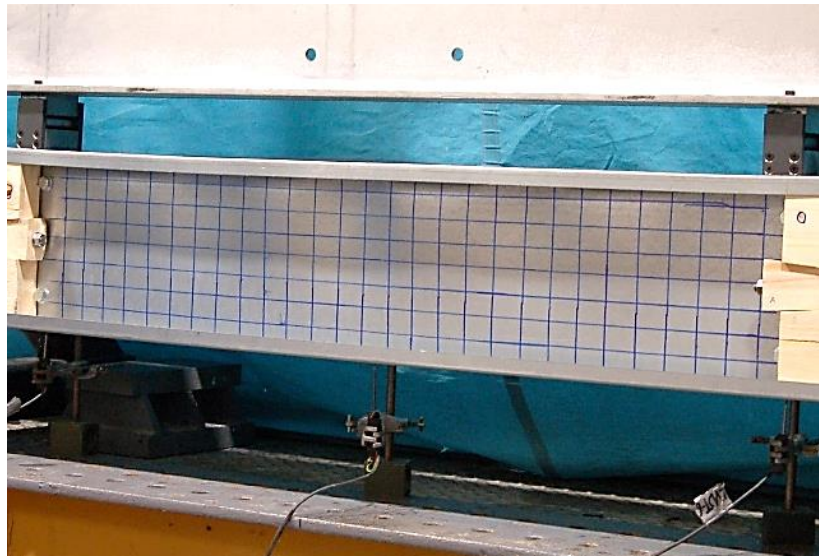
Fig. 20: Buckling pattern in specimen B270-2
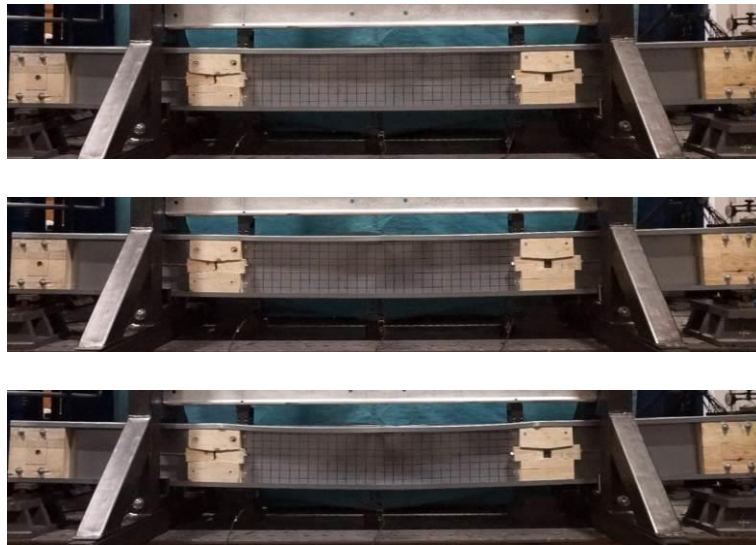
Fig. 21: Progressive deformations of beam B270-2
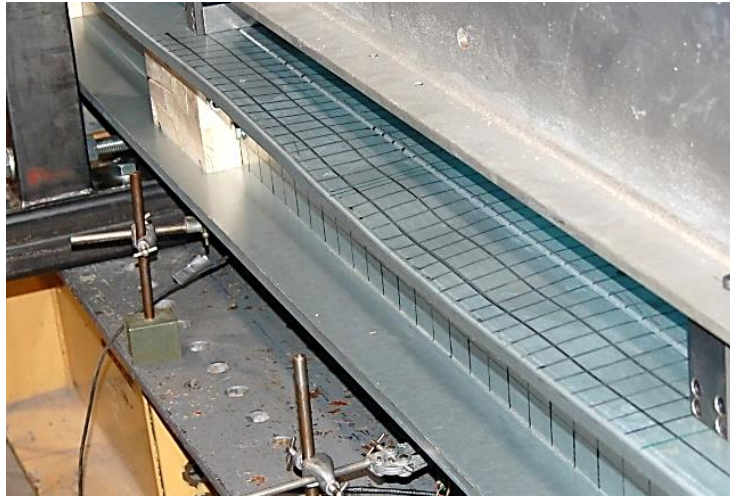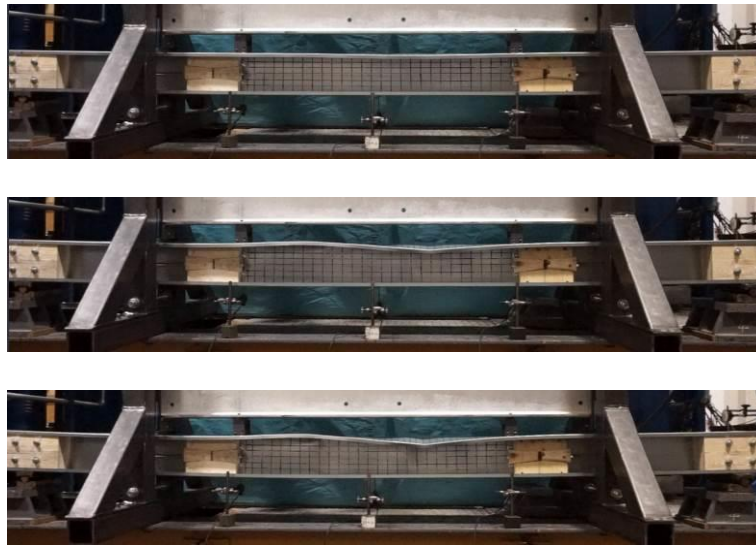
Fig. 22: Buckling pattern in specimen C180-1

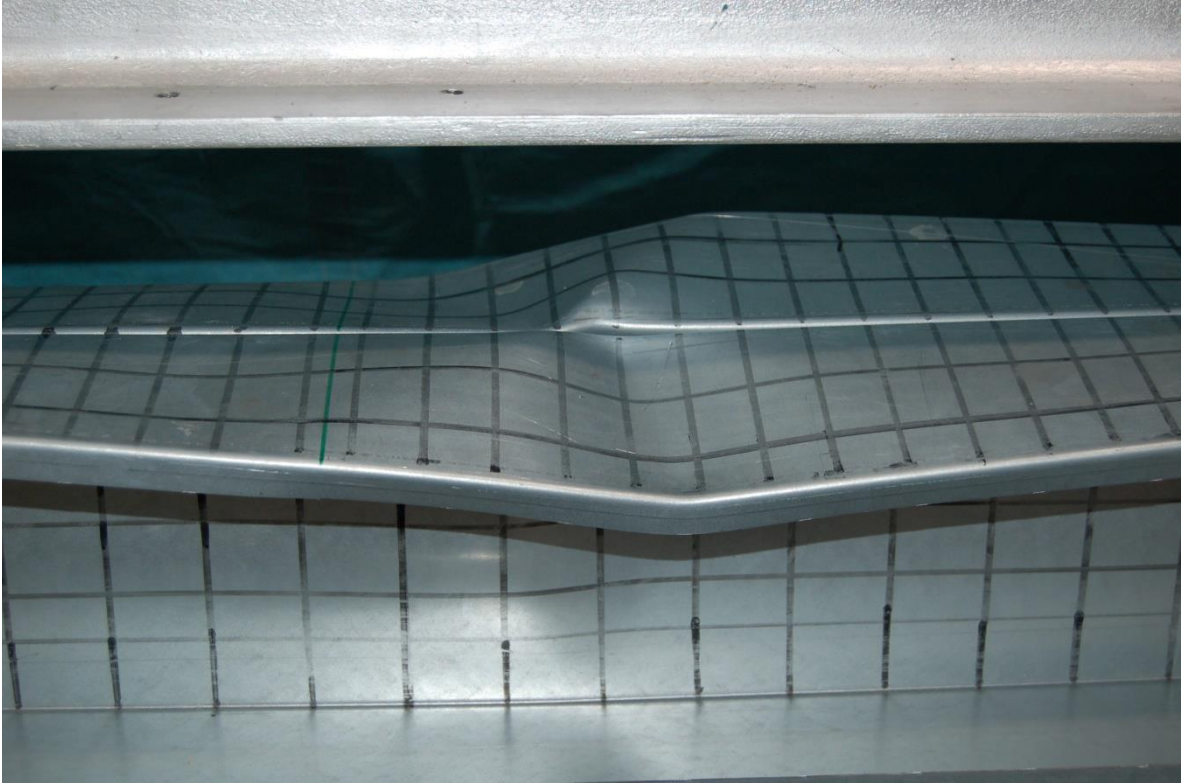Fig. 23: Progressive deformations of beam C180-2
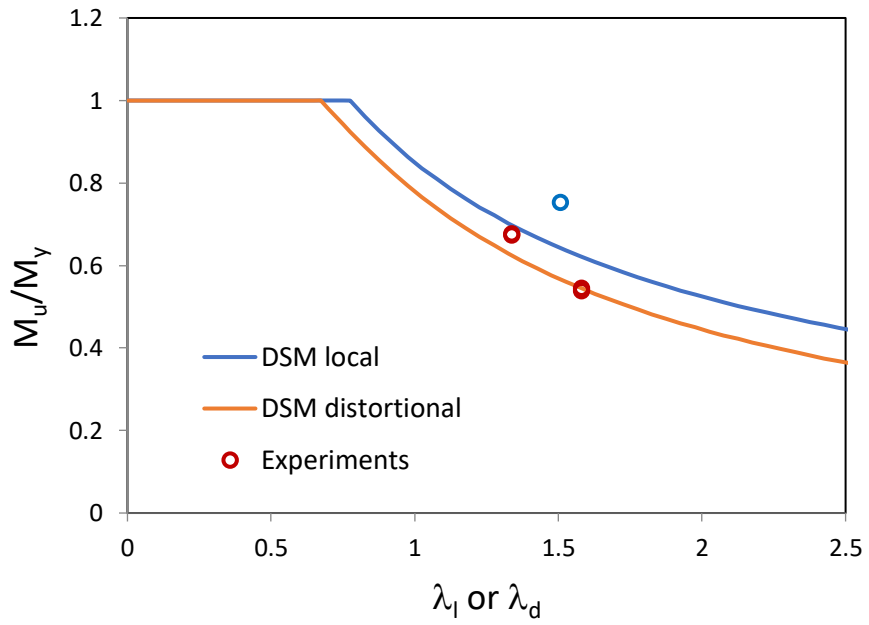
Fig. 24: Localization of the buckling pattern into yield lines

Fig. 25: Comparison of test results with current DSM design rules